Computers and Fluids 146 (2017) 105–116

Contents lists available at ScienceDirect

Computers and Fluids

journal homepage: www.elsevier.com/locate/compfluid

Numerical simulations of compressible multicomponent and multiphase flow using a high-order targeted ENO (TENO) finite-volume method

Ory Haimovich*, Steven H. Frankel

Faculty of Mechanical Engineering, Technion Israel Institute of Technology, Haifa 32000, Israel

ARTICLE INFO

Article history:
Received 29 May 2016
Revised 28 November 2016
Accepted 14 January 2017
Available online 16 January 2017

Keywords:
Multiphase flow
High-order scheme
WENO
Two-phase model
Shock-bubble interaction

ABSTRACT

High-order numerical simulations of compressible multicomponent and multiphase flows are challenging due to the need to resolve both complex flow features and sharp gradients associated with material interfaces or shocks with minimal spurious oscillations. Recently, in the context of the WENO family of schemes, increasing the ENO property and incorporating improved convergence properties near local extrema points, has resulted in the targeted ENO or TENO scheme. In this study, a robust high-order finite-volume method based on the TENO scheme is implemented and tested for simulating multicomponent and multiphase compressible flows. A fifth-order spatial reconstruction is combined with a high-resolution modified HLLC Riemann solver, adjusted for the six-equation formulation of the diffuse interface model, and a third-order TVD Runge–Kutta explicit time-stepping scheme. Multidimensional extension is handled utilizing Gauss–Legendre quadrature points to evaluate both the flux and gas void fraction inter-cell terms. Several challenging 1D and 2D test cases are performed and compared to previously published experimental data and numerical simulations where available. A parametric study of the user-defined threshold parameter in the TENO algorithm is also studied and the TENO scheme is found to be more robust and less dissipative than both the WENO-Z and WENO-JS schemes.

© 2017 Elsevier Ltd. All rights reserved.

1. Introduction

Multicomponent and multiphase compressible flows are widely found in science and engineering such as astrophysics, combustion, explosions, detonations, nuclear reactors, and underwater projectiles. These highly turbulent flows often feature interactions between shock waves and bubbles related to cavitation. The challenge in high-fidelity numerical simulation of such flows is to accurately resolve turbulent flow features while simultaneously providing targeted dissipation to avoid spurious oscillations associated with capturing shocks and sharp interfaces.

There are two main approaches to mathematically modeling and numerical simulating high-speed two-phase flows regarding how they treat the two-phase interface. Sharp interface methods (SIM) explicitly detect and treat discontinuities. Examples include Lagrangian methods, which are comprehensively reviewed by Benson [5], volume-of-fluid (VOF) methods, presented for compressible flows by Miller and Puckett [30], front-tracking methods as described by Cocchi and Saurel [9], and Arbitrary-Lagrangian Eulerian (ALE) methods, formulated for multifluid flow by Luo et al. [28]. The main disadvantages of SIM includes complex implementation, large computational expense, issues related to conservation of physical quantities near the interfaces, and inability to dynamically create new interfaces in cavitating flows [38].

Alternatively, diffuse interface methods (DIM), treat the interface as a diffuse zone, allowing the solution of a single global set of governing equations over the entire computational domain. DIM naturally captures the multispecies or multiphase interface, including all generated waves, with specifying interface information as needed by SIM. Challenges related to handling phase interactions remain and are often accounted for using an averaging approach to derive appropriate multifluid system equations and resulting in interphase mass, momentum, and energy source terms [13]. Saurel and Abgrall [37] derived a full non-equilibrium model, consisting of seven equations in one-dimension e.g. balance equations for mass, momentum and energy of each phase and a supplementary transport equation for the void fraction of one of the phases. The six-equation model, which is widely used in industrial and commercial codes, e.g. CATHARE [6], is known to be ill-posed in the sense that the model has complex eigenvalues, as noted by Stewart and Wendroff [40]. Bestion [6] managed to recover system

* Corresponding author.
E-mail address: ory.haimovich@gmail.com (O. Haimovich).

http://dx.doi.org/10.1016/j.compfluid.2017.01.012
0045-7930/© 2017 Elsevier Ltd. All rights reserved.

hyperbolicity by modifying the interfacial pressure. Chang and Liou [8] adjusted the AUSM+up Riemann solver for the six-equation model and Yeom and Chang [45,46] implemented HLL and HLLC-type solvers in the same context.

Further reduction of the number of governing equations is also possible by taking the asymptotic limit of zero relaxation time for both velocity and pressure relaxation processes valid as in the seven-equation model of Kapila et al. [24]. It is noteworthy to mention that this model contains a transport equation for the void fraction which has a non-conservative term and results in a non-monotonic mixture sound speed. Another form of this model, derived by Allaire et al. [2], corresponds to multicomponent problems, and Perigaud and Saurel [34] incorporated viscous and surface tension terms. Recently, Coralic and Colonius [10] employed a fifth-order WENO scheme for the reduced five equation multicomponent formulation.

Numerical simulations of flows with high gradients of density, pressure, and velocity, such as vortical flows with shocks, benefit from high-order non-oscillatory schemes especially near high-gradients. Total variation diminishing (TVD) schemes have been widely developed for second-order spatial methods. However, TVD schemes degenerate to first-order locally in the vicinity of critical points and are considered to be too dissipative to capture fine flow details. Attempts to obtain high order non-oscillatory schemes were pioneered by Harten et al. [20]. Essentially non-oscillatory (ENO) schemes employ the smoothest among r candidate stencils to serve as rth-order interpolation functions. In the weighted essentially non-oscillatory (WENO) method [22], a convex combination of r candidate stencils are used to achieve $(2r-1)$th-order approximations in smooth regions and having the desired property of being non-oscillatory in the vicinity of high gradients. The later property is achieved by introducing smoothness indicators to reduce the influence of stencils containing high gradients while retaining the original value of the ideal weights. In cases where all candidate stencils contain discontinuities, locating at least one smooth stencil is not possible and the ENO property cannot be enforced. One possible way to deal with this problem is through the use of monotonicity-preserving WENO (MPWENO) scheme [4], at the price of added dissipation.

The WENO-M scheme, devised by Henrick et al. [21], deals with the fact that around critical points the WENO-JS scheme fails to retain its design order of accuracy. They proposed a mapping function applied to the non linear weights to address this and preserve optimal accuracy even if the first or higher derivatives vanish. It is noteworthy that WENO-M schemes enhances the importance of stencils containing discontinuities. As a result, less accurate results may be achieved for long time simulation as demonstrated by Feng et al. [14] who developed a new mapping function to reduce the influence of non-smooth stencils. Alternatively, Borges et al. [7] suggested use of a novel smoothness indicator, linearly related to the global stencil but including all candidate stencils, also known as WENO-Z. They were able to improve local accuracy near critical points and demonstrated improved results compared to WENO-JS and WENO-M.

Despite all of the above research, capturing fine flow details may lead to undesirable situations where discontinuities are still present within all candidate stencils in any of the above algorithms. This suggests the guiding principle of retaining the ENO property near high gradients and still using a high-order scheme as much as possible. Recently, Fu et al. [15], formulated a novel concept named targeted ENO or TENO, utilizing the WENO-Z method and disregarding the influence of stencils containing discontinuities with ENO-like stencil selection. This results in a scheme with increased robustness and the ability to capture fine-scale details with multiple discontinuities within each global interpolation stencil while retaining sufficient spectral resolution

In the present paper, a 5th-order spatial reconstruction scheme is developed using the TENO scheme in the context of a finite-volume formulation for both multicomponent and multiphase flows. A high-resolution HLLC approximate Riemann solver, adjusted for multiphase problems [46] with multidimensional extension using Gauss–Legendre quadrature points [42] is utilized. A 3rd-order TVD explicit Runge–Kutta scheme is used for time stepping [16].

The paper continues below with Section 2 which presents the governing equations of the problem including details regarding the interfacial source terms and primitive variables decomposition. Section 3 is devoted to the details of the implementation of the high-order TENO spatial reconstruction and multidimensional flux evaluation Riemann solver. In Section 4, results from several benchmark cases including cavitation test case, shock-tube problem, shock-bubble interaction and underwater explosion are presented. Concluding remarks are given in Section 5.

2. Mathematical formulation

2.1. Governing equations

Here we consider the six-equation, two-fluid model of Yeom and Chang [46] which features inviscid balance equations for mass, momentum, and energy of each phase:

$$\frac{\partial \mathbf{U}_k}{\partial t}+\frac{\partial \mathbf{F}_k}{\partial x}+\mathbf{H}(\mathbf{U}_k)\frac{\partial \alpha_g}{\partial x}+\frac{\partial \mathbf{G}_k}{\partial y}+\mathbf{I}(\mathbf{U}_k)\frac{\partial \alpha_g}{\partial y}=\mathbf{S}_k(\mathbf{U}_k) \tag{1}$$

where $k=g,l$ correspond to the gas and liquid phases, respectively, and the following vectors are defined as:

$$\mathbf{U}_k=\begin{pmatrix}\alpha\rho\\ \alpha\rho u\\ \alpha\rho v\\ \alpha\rho E\end{pmatrix}_k;\ \mathbf{F}_k=\begin{pmatrix}\alpha\rho u\\ \alpha\rho u^2+\alpha P\\ \alpha\rho uv\\ \alpha u(\rho E+P)\end{pmatrix}_k;\ \mathbf{G}_k=\begin{pmatrix}\alpha\rho v\\ \alpha\rho uv\\ \alpha\rho v^2+\alpha P\\ \alpha v(\rho E+P)\end{pmatrix}_k \tag{2}$$

$$\mathbf{H}_k=\begin{pmatrix}0\\ -P^{int}\\ 0\\ -P^{int}u^{int}\end{pmatrix}_k;\ \mathbf{I}_k=\begin{pmatrix}0\\ 0\\ -P^{int}\\ -P^{int}v^{int}\end{pmatrix}_k;\ \mathbf{S}_k=\begin{pmatrix}0\\ F_x^D\\ F_y^D\\ u^{int}F_x^D+v^{int}F_y^D\end{pmatrix}_k \tag{3}$$

where U is the conservative state vector, F and G are the inviscid flux vectors, and H and I are the non-conservative vectors in the x and y directions, respectively.

The primitive variables here are the void fraction, density, x and y velocity components, total energy per mass, and pressure, denoted as: α, ρ, u, v, E and P, respectively. Further, P^{int} is the interfacial pressure, u^{int} and v^{int} are the x and y interfacial velocity components, respectively, and F^D is the interfacial drag force. Enforcing pressure equilibrium e.g. $P_g=P_l=P$, a physical constraint on the void fractions $\alpha_g+\alpha_l=1$, and using a corresponding stiffened-gas equation of state for each phase, allows closure to the given system.

2.2. Interfacial terms

The above governing equations system, Eq. (1), are known to be ill-posed as a result of their complex system eigenvalues. This may eventually lead to the onset of artificial numerical instabilities. To remedy this and recover hyperbolicity, e.g. real eigenvalues, it was suggested by Stuhmiller [41] to modify the interfacial pressure, P^{int}, in the following way:

$$P^{int}=P-\delta\frac{\alpha_g\alpha_l\rho_g\rho_l}{\alpha_g\rho_l+\alpha_l\rho_g}(u_g-u_l)^2 \tag{4}$$

where hyperbolicity is guaranteed if $\delta \geq 1$. In our work, we follow Chang and Liou [8] and choose $\delta = 2$. Saurel and Abgrall [37] assumed velocity equilibrium at the center of mass for phase velocities to obtain the following estimates of the interfacial velocities u^{int} and v^{int}:

$$u^{int} = \frac{\alpha_g \rho_g u_g + \alpha_l \rho_l u_l}{\alpha_g \rho_g + \alpha_l \rho_l} \tag{5a}$$

$$v^{int} = \frac{\alpha_g \rho_g v_g + \alpha_l \rho_l v_l}{\alpha_g \rho_g + \alpha_l \rho_l} \tag{5b}$$

2.3. Equation of state

As mentioned, a stiffened-gas equation of state (EOS), introduced by Harlow and Amsden [19], is used for each phase to achieve closure:

$$P_k = (\gamma_k - 1)\rho_k e_k - \gamma_k P_{\infty,k} \tag{6}$$

here e is the specific internal energy, satisfying the equation $e = E - \frac{1}{2}\left(u^2 + v^2\right)$, with fitting parameters γ and $P_{\infty,k}$. The speed of sound of each phase is defined by:

$$c_k = \sqrt{\frac{\gamma_k (P_k + P_{\infty,k})}{\rho_k}} \tag{7}$$

2.4. Decomposition of primitive variables

At the end of each Runge–Kutta stage, the primitive variables need to be recalculated. To illustrate this the following notation is used to denote the conservative vector components for each phase:

$$U = \begin{pmatrix} \alpha\rho \\ \alpha\rho u \\ \alpha\rho v \\ \alpha\rho E \end{pmatrix}_k = \begin{pmatrix} \mathcal{M} \\ \mathcal{U} \\ \mathcal{V} \\ \mathcal{E} \end{pmatrix}_k \tag{8}$$

Using the EOS of each phase, the void fraction can be written:

$$\alpha_k = \frac{(\gamma_k - 1)(\mathcal{E}_k - \frac{\mathcal{U}_k^2 + \mathcal{V}_k^2}{2\mathcal{M}_k})}{P_k + \gamma_k P_{\infty,k}} \tag{9}$$

By substituting these expressions into the void fraction constraint and recalling the pressure equilibrium assumption, the following quadratic equation for the pressure is obtained:

$$P^2 + (\mathcal{B} - \mathcal{A})P - \mathcal{A}\mathcal{C} = 0 \tag{10}$$

where:

$$\mathcal{A} = (\gamma_g - 1)\left(\mathcal{E}_g - \frac{\mathcal{U}_g^2 + \mathcal{V}_g^2}{2\mathcal{M}_g}\right) \tag{11}$$

$$\mathcal{B} = -(\gamma_l - 1)\left(\mathcal{E}_l - \frac{\mathcal{U}_l^2 + \mathcal{V}_l^2}{2\mathcal{M}_l}\right) + \gamma_l P_{\infty,l} \tag{12}$$

$$\mathcal{C} = \gamma_l P_{\infty,l} \tag{13}$$

where its positive roots serve as initial guesses for a Newton–Raphson algorithm applied on the two corresponding equations of void fraction expressions simultaneously:

$$\alpha_g P - (\gamma_g - 1)\left(\mathcal{E}_g - \frac{\mathcal{U}_g^2 + \mathcal{V}_g^2}{2\mathcal{M}_g}\right) = 0 \tag{14a}$$

$$\alpha_l\left(P + \gamma_l P_{\infty,l}\right) - (\gamma_l - 1)\left(\mathcal{E}_l - \frac{\mathcal{U}_l^2 + \mathcal{V}_l^2}{2\mathcal{M}_l}\right) = 0 \tag{14b}$$

3. Numerical method

The hyperbolic part of the governing equations is written here as:

$$\frac{\partial \mathbf{U}}{\partial t} + \frac{\partial \mathbf{F}}{\partial x} + \frac{\partial \mathbf{G}}{\partial y} = \mathbf{H}(\mathbf{U})\frac{\partial \alpha_g}{\partial x} + \mathbf{I}(\mathbf{U})\frac{\partial \alpha_g}{\partial y} \tag{15}$$

Integration of Eq. (15) over an arbitrary cell area $\mathcal{I}_{ij}$ in $x-y$ plane described by:

$$\mathcal{I}_{ij} = [x_{i-1/2}, x_{i+1/2}] \times [y_{j-1/2}, y_{j+1/2}]$$

where $x_{i \pm 1/2}$ and $y_{j \pm 1/2}$ represent cell faces positions of a given computational cell with grid spacing $\Delta x = x_{i+1/2} - x_{i-1/2}$ and $\Delta y = y_{j+1/2} - y_{j-1/2}$.

We denote by θ and ϑ the discrete form of $\frac{\partial \alpha_g}{\partial x}$ and $\frac{\partial \alpha_g}{\partial y}$, respectively. Derivation of the term θ is obtained by explicitly writing the semi-discrete form, of both the mass and momentum conservation equations for the one-dimensional case:

$$\frac{d(\alpha_k \rho_k)_i}{dt} = -\frac{1}{\Delta x}\left[(\alpha_k \rho_k u_k)^*_{i+1/2} - (\alpha_k \rho_k u_k)^*_{i-1/2}\right] \tag{16}$$

$$\frac{d(\alpha_k \rho_k u_k)_i}{dt} = -\frac{1}{\Delta x}\left[\left(\alpha_k \rho_k u_k^2 + \alpha_k P_k\right)^*_{i+1/2} - \left(\alpha_k \rho_k u_k^2 + \alpha_k P_k\right)^*_{i-1/2}\right] + \Delta t \cdot P^{int} \cdot \theta \tag{17}$$

Recall the uniform pressure and velocity principle, originally proposed by Abgrall [1], namely assuming uniform profiles of velocity and pressure would remain the same. As a result, we substitute $P^{int} = P^*_{i+1/2} = P^*_{i-1/2} = P$ and $u^*_{i+1/2} = u^*_{i-1/2} = u$ in Eqs. (16) and (17), and subtract $u \times$ Eq. (16) from Eq. (17). As a result the mathematical expression for θ is :

$$\theta = \frac{(\alpha_g)^*_{i+1/2} - (\alpha_g)^*_{i-1/2}}{\Delta x} \tag{18}$$

where:

$$(\alpha_g)^*_{i+1/2} = \left(\alpha_k \rho_k u_k^2 + \alpha_k P\right)^*_{i+1/2} - (\alpha_k \rho_k u_k)^*_{i+1/2} \tag{19}$$

ϑ is derived in a straightforward way, and we present the semi-discrete form of Eq. (15):

$$\frac{d\mathbf{U}_{i,j}}{dt} = \frac{1}{\Delta x}\left[\mathbf{F}^*_{i-1/2,j} - \mathbf{F}^*_{i+1/2,j}\right] + \frac{1}{\Delta y}\left[\mathbf{G}^*_{i,j-1/2} - \mathbf{G}^*_{i,j+1/2}\right] + \frac{1}{\Delta x}\mathbf{H}(\mathbf{U}_{i,j})\left[(\alpha_g)^*_{i-1/2,j} - (\alpha_g)^*_{i+1/2,j}\right] + \frac{1}{\Delta y}\mathbf{I}(\mathbf{U}_{i,j})\left[(\alpha_g)^*_{i,j-1/2} - (\alpha_g)^*_{i,j+1/2}\right] \tag{20}$$

where $\mathbf{F}^*_{i+1/2,j}$ and $(\alpha_g)^*_{i+1/2,j}$ are the x-direction numerical flux and gas void fraction spatial averages, respectively, evaluated over the transverse cell interface and written as:

$$\mathbf{F}^*_{i+1/2,j} = \frac{1}{\Delta y}\int_{y_{j-1/2}}^{y_{j+1/2}} \mathbf{F}(\mathbf{U}(x_{i+1/2}, y, t))dy \tag{21}$$

$$(\alpha_g)^*_{i+1/2,j} = \frac{1}{\Delta y}\int_{y_{j-1/2}}^{y_{j+1/2}} \alpha_g(x_{i+1/2}, y, t)dy \tag{22}$$

and the expressions for $\mathbf{G}^*_{i,j+1/2}$ and $\left(\alpha_g\right)^*_{i,j+1/2}$ are derived in a similar way.

We now proceed with obtaining a numerical approximation to the exact relation of the semi-discrete formulation. We follow the implementation of a two-point, forth-order accurate approximation by Gaussian–Legendre quadrature rule, as suggested by Titarev and

Toro [42] for evaluating the flux integral at the cell face:

$$\mathbf{F}^*_{i+1/2,j} = \frac{1}{2}\sum_{l=1}^{2}\mathbf{F}(\mathbf{U}(x_{i+1/2}, y_{jl}, t)) \tag{23}$$

where the Gaussian points are $y_{j,1,2} = y_j \pm \frac{\Delta y_j}{2\sqrt{3}}$.

We utilize the recently published fifth-order TENO scheme, to reconstruct cell average values to evaluation (Gaussian) points in order to achieve high-order approximations of Eq. (20). In the finite volume concept, at each cell interface, there are left and right state values. As a consequence, we apply a suitable monotone function to evaluate each flux. The modified HLLC approximate Riemann solver, adjusted and validated by Yeom and Chang [46], has been implemented and hence Eq. (23) can be written:

$$\mathbf{F}^*_{i+1/2,j} = \frac{1}{2}\sum_{l=1}^{2}\mathbf{F}^{HLLC}(\mathbf{U}^L(x_{i+1/2}, y_{jl}, t), \mathbf{U}^R(x_{i+1/2}, y_{jl}, t)) \tag{24}$$

To solve the two-dimensional governing equations, Eq. (20), we apply a local one-dimensional approximate Riemann solver at each cell interface, consisting of two non-linear waves, a contact discontinuity wave and a shear wave. Hereafter, we give details regarding implementation of high-order reconstruction and flux evaluation for the x-direction, namely evaluating $F^*_{i+1/2,j}$, whereas evaluating the transverse flux, $G^*_{i,j+1/2}$, is done in a similar manner.

3.1. High-order reconstruction

It was demonstrated by Johnsen and Colonius [23] that reconstructing primitive variables rather than conservative variables, may prevent the undesirable evolution of oscillations near interfaces. Consequently, in this paper, we implement a fifth-order spatial scheme by reconstructing primitive variables on the cell faces using the TENO [15] scheme. In the study of Fu et al. [15], fifth-order convergence of the TENO scheme was demonstrated for the linear advection problem. Recalling the fact that the six equation model has complex eigenvalues and only approximate expressions can be derived, hence using characteristic decomposition, as suggested by Titarev and Toro [42], is not applicable within the current framework.

For a fifth-order spatial reconstruction, the three candidate stencils with respect to a given computational cell, $[x_{i-1/2}, x_{i+1/2}]$, are:

$$S_0 = (i, i+1, i+2); \quad S_1 = (i-1, i, i+1); \quad S_2 = (i-2, i-1, i) \tag{25}$$

The fifth-order approximations for the left and right faces in a given cell, respectively, are:

$$V^L_{i+1/2} = \frac{\omega_0}{6}[2V_i + 5V_{i+1} - V_{i+2}] + \frac{\omega_1}{6}[-V_{i-1} + 5V_i + 2V_{i+1}] + \frac{\omega_2}{6}[2V_{i-2} - 7V_{i-1} + 11V_i] \tag{26}$$

$$V^R_{i-1/2} = \frac{\omega_0}{6}[11V_i - 7V_{i+1} + 2V_{i+2}] + \frac{\omega_1}{6}[2V_{i-1} + 5V_i - V_{i+1}] + \frac{\omega_2}{6}[-2V_{i-2} + 5V_{i-1} + 2V_i] \tag{27}$$

Further details regarding the WENO weights are given in Appendix A. The nonlinear weights, inspired by WENO-Z [7] scheme, with increased scale separation [15] are:

$$\gamma_k = \left[1 + \frac{\tau_5}{\beta_k + \epsilon}\right]^6, \quad k = 0, 1, 2. \tag{28}$$

where $\tau_5 = |\beta_2 - \beta_0|$ is the global smoothness indicator introduced by Borges et al. [7]. Also, β_k is the smoothness indicator of each candidate stencil, introduced by Jiang and Shu [22]:

$$\beta_0 = \frac{13}{12}(V_i - 2V_{i+1} + V_{i+2})^2 + \frac{1}{4}(3V_i - 4V_{i+1} + V_{i+2})^2 \tag{29a}$$

$$\beta_1 = \frac{13}{12}(V_{i-1} - 2V_i + V_{i+1})^2 + \frac{1}{4}(V_{i-1} - V_{i+1})^2 \tag{29b}$$

$$\beta_2 = \frac{13}{12}(V_{i-2} - 2V_{i-1} + V_i)^2 + \frac{1}{4}(V_{i-2} - 4V_{i-1} + 3V_i) \tag{29c}$$

In what follows, we normalize the non-linear weights

$$\chi_k = \frac{\gamma_k}{\sum_{l=0}^{l=2}\gamma_k} \tag{30}$$

and employ an ENO-like stencil selection utilizing a user-defined threshold parameter, C_T, in the following way:

$$\delta_k = \begin{cases} 0, & \text{if } \chi_k < C_T \\ 1, & \text{else} \end{cases} \tag{31}$$

By doing so, we guarantee the contribution of non-smooth stencils is zero, thus preventing interpolation across discontinuities and retaining high accuracy to a maximal extent. The new non-linear weights are given as:

$$\omega_k = \frac{d_k\delta_k}{\sum_{l=0}^{l=2} d_l\delta_l} \tag{32}$$

where d_l are the ideal weights, equal to $d_0 = \frac{3}{10}$, $d_1 = \frac{6}{10}$ and $d_2 = \frac{1}{10}$ to obtain the left side value. The ideal weights correspond to the right side cell face are derived in a symmetric way.

3.2. Approximate Riemann solver

As mentioned before, an approximate HLLC Riemann solver is used here incorporating the two non-linear fastest waves, similar to HLL solver, and restoring the contact discontinuity wave, in the following way for two-phase formulation:

$$(F)^{HLLC}_{i+1/2} = \begin{cases} F_L & \text{if } S_L \geq 0 \\ F_L + S_L(\mathbf{U}^*_L - \mathbf{U}_L) & \text{if } S_L \leq 0 \leq S^* \\ F_R + S_R(\mathbf{U}^*_R - \mathbf{U}_R) & \text{if } S^* \leq 0 \leq S_R \\ F_R & \text{if } S_R \leq 0 \end{cases} \tag{33}$$

Generally, the intermediate state vector incorporates the intermediate vector of each phase, in the following way:

$$\mathbf{U}^*_D = \begin{pmatrix} \mathbf{U}^*_{Dg} \\ \mathbf{U}^*_{Dl} \end{pmatrix}$$

where $D = L, R$ corresponds to left and right faces at a given interface, respectively, and the intermediate state vector of each phase is:

$$\mathbf{U}^*_{DK} = \frac{\alpha_{DK}\rho_{DK}(S_{DK} - u_{DK})}{S_{DK} - S^*}\begin{pmatrix} 1 \\ S^* \\ v_D \\ E_{DK} + (S^* - u_{DK}[S^* + \frac{P_{DK}}{\rho_{DK}(S_{DK} - u_{DK})}]) \end{pmatrix} \tag{34}$$

We further simplify the mathematical expression of the gas void fraction at the cell face, $(\alpha_g)^*_{i+1/2}$, given in Eq. (19), by substituting the corresponding components taken from the HLLC solver, Eq. (33):

$$(\alpha_g)^*_{i+1/2} = \begin{cases} (\alpha_g)^L_{i+1/2} & \text{if } S^* \geq 0 \\ (\alpha_g)^R_{i+1/2} & \text{otherwise} \end{cases}$$

We follow Davis' waves estimation [11] and the two-phase adaptation of Zein et al. [47] to approximate the left and right fastest waves:

$$S_L = min(u_{gL} - c_{gL}, u_{lL} - c_{lL}, u_{gR} - c_{gR}, u_{lR} - c_{lR}) \tag{35a}$$

$$S_R = max(u_{gL} + c_{gL}, u_{lL} + c_{lL}, u_{gR} + c_{gR}, u_{lR} + c_{lR}) \tag{35b}$$

and the intermediate wave speed S^* following Toro [43] is given by:

$$S^* = \frac{\bar{P}_R - \bar{P}_L + \bar{\rho}_L \bar{u}_L (S_L - \bar{u}_L) - \bar{\rho}_R \bar{u}_R (S_R - \bar{u}_R)}{\bar{\rho}_L (S_L - \bar{u}_L) - \bar{\rho}_R (S_R - \bar{u}_R)} \tag{36}$$

with the pressure, density, and velocity mixture values given as:

$$\bar{P}_D = \alpha_{gD} P_{gD} + \alpha_{lD} P_{lD} \tag{37a}$$

$$\bar{\rho}_D = \alpha_{gD} \rho_{gD} + \alpha_{lD} \rho_{lD} \tag{37b}$$

$$\bar{u}_D = \frac{\alpha_{gD} \rho_{gD} u_{gD} + \alpha_{lD} \rho_{lD} u_{lD}}{\bar{\rho}_D} \tag{37c}$$

3.3. Time stepping

Besides implementing spatially high-order discretization, high-order time stepping is considered here as well. Hence, the 3rd-order TVD Runge–Kutta time stepping algorithm of Gottlieb and Shu [16] is implemented:

$$\mathbf{U}^{(1)}_{i,j} = \mathbf{U}^{n}_{i,j} + \Delta t L\left(\mathbf{U}^{n}_{i,j}\right) \tag{38a}$$

$$\mathbf{U}^{(2)}_{i,j} = \frac{3}{4}\mathbf{U}^{n}_{i,j} + \frac{1}{4}\mathbf{U}^{(1)}_{i,j} + \frac{1}{4}\Delta t L\left(\mathbf{U}^{(1)}_{i,j}\right) \tag{38b}$$

$$\mathbf{U}^{n+1}_{i,j} = \frac{1}{3}\mathbf{U}^{n}_{i,j} + \frac{2}{3}\mathbf{U}^{(2)}_{i,j} + \frac{2}{3}\Delta t L\left(\mathbf{U}^{(2)}_{i,j}\right) \tag{38c}$$

where $L(\mathbf{U}_{i,j})$ is the spatial operator corresponding to the right hand side of Eq. (20), at the relevant time step.

The local time step in each direction is calculated based on the definition of the CFL number as shown for the 1D case here:

$$(\Delta t)_i = CFL \cdot \frac{\Delta x}{\lambda_{max}} \tag{39}$$

where λ_{max} is the maximum eigenvalue of an approximated Jacobian matrix following the approach of Yeom and Chang [45]. It is straightforward to show that the eigenvalues are bounded by their corresponding single-phase values. Hence, the maximum eigenvalue is computed according to:

$$\lambda_{max} = \max_k \left(|u_k| + c_k\right) \tag{40}$$

The time step is then selected as the minimum over the entire computational domain according to:

$$\Delta t = \min_{0 \le i \le N-1} \left((\Delta t)_i\right) \tag{41}$$

3.4. Algorithm summary

A summary of the above described algorithm is given here:

1. Reconstruct high-order approximation of left and right primitive state vector at cell face $i+1/2$ using TENO algorithm, applied on cell average values from $i-2$ to $i+2$
2. Apply TENO scheme on cell faces values to obtain high-order approximations on Gauss–Legendre quadrature points
3. Compute fluxes at Gauss–Legendre points using a modified HLLC approximate Riemann solver
4. Apply high-order integration rule to calculate the flux at the cell face $i+1/2$
5. Simultaneously, apply steps (1)–(4) to reconstruct the void fraction cell face value
6. Repeat steps (1)–(5) to obtain all fluxes within a given computational cell
7. Substitute fluxes in the semi-discrete form of the governing equations, Eq. (20)

Table 1
Gas void fraction convergence study after one time period using 5th-order Targeted-ENO scheme.

Mesh	L_1 norm	L_1 order	L_∞ norm	$L\infty$ order
25	$4.528 \cdot 10^{-2}$	–	$2.450 \cdot 10^{-3}$	–
50	$8.915 \cdot 10^{-3}$	2.345	$2.261 \cdot 10^{-4}$	3.437
100	$6.445 \cdot 10^{-4}$	3.790	$8.329 \cdot 10^{-6}$	4.763
200	$3.621 \cdot 10^{-5}$	4.154	$2.965 \cdot 10^{-7}$	4.812

4. Numerical results

Results of several standard yet challenging 1D and 2D problems are presented here. First, results from a convergence study are presented to demonstrated the schemes high-order of accuracy. A 1D cavitation benchmark case and multiphase shock-tube problems are considered first to demonstrate the capabilities of TENO scheme in comparison with other schemes in the WENO family. The multiphase advection problem is simulated to demonstrate the interface capturing ability of the proposed scheme without introducing artificial oscillations and still being less dissipative than WENO-JS. The Helium/air multicomponent and water/air multiphase shock-bubble interaction problems are also studied. Simulations of underwater explosion problems near a water-air surface and under a rigid solid surface are also studied.

4.1. Convergence study

The high-order convergence property of the scheme is demonstrated by considering advection of a smooth profile for the gas void fraction. The convergence study of Greenough and Rider [17], who considered a Gaussian profile for the density, motivates our choice of a similar profile for the void fraction, here:

$$\alpha_g = 0.5 + 0.02 \exp((x - 0.5)^2 / 2\delta^2) \tag{42}$$

where $\delta = 0.0625$, with a given constant velocity $u = 10;\text{m/s}$ and $CFL = 0.8$. The computational domain is [0, 1] with periodic boundary conditions, and both L_1 and L_∞ norms of the gas void fraction profile are compared after one time period, namely at $t = 0.1;\text{s}$. The pressure is uniform and set as $P = 101325;\text{Pa}$, with EOS parameters of air and water: $\gamma_g = 1.4$, $P_{\infty,g} = 0$, $\gamma_l = 1.932$, $P_{\infty,l} = 1.1645 \cdot 10^9;\text{Pa}$. It is noteworthy that the full six-equation formulation is being solved in this convergence study and the initial void fraction profile was selected so as to activate the differential source term $P\frac{\partial \alpha_g}{\partial x}$.

The results of the convergence study for the 5th-order Targeted-ENO scheme are summarized in Table 1, where L_1 and L_∞ norm of gas void fraction cell average values are presented. From these results an approximate fifth-order convergence is demonstrated.

4.2. Cavitation test case

In the second test case, originally proposed by Saurel and Abgrall [37] and further explored by Saurel and Lemetayer [38], Yeom and Chang [46], and Daramizadeh and Ansari [12], a velocity discontinuity is imposed at the center of a 1-m long tube filled with

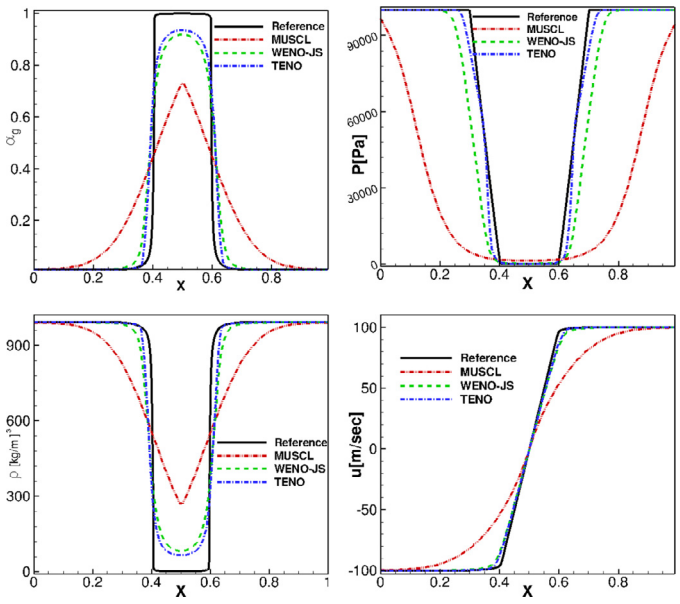

Fig. 1. Comparison between 5th-order TENO with $C_T = 10^{-7}$, 5th-order WENO-JS, and 3rd-order MUSCL with reference solution at $t = 1$ ms, 100 computational cells and $CFL = 0.8$ for a one-dimensional cavitation test problem showing axial profiles of α_g, gas void fraction, P, pressure, ρ, mixture density and u, velocity.

liquid water which results in cavitation due to the presence of rarefaction waves. The initial gas void fraction is chosen to be 0.01 along the entire computational domain and the initial left and right state vectors are:

$$(P, \alpha_g, \rho_g, \rho_l, u_g, u_l)_L = (10^5, 0.01, 50, 1000, -100, -100)$$

$$(P, \alpha_g, \rho_g, \rho_l, u_g, u_l)_R = (10^5, 0.01, 50, 1000, 100, 100)$$

In order to physically keep the velocity at zero in the center of the domain, the local pressure has to decrease as result of cavitation onset. The EOS parameters for this case are: $\gamma_g = 1.4$, $P_{\infty,g} = 0$ and $\gamma_l = 1.932$, $P_{\infty,l} = 1.1645 \cdot 10^9$ Pa, for vapor and liquid water, respectively.

Results obtained using the 5th-order TENO scheme with $C_T = 10^{-7}$, the 5th-order WENO-JS scheme, and the 3rd-order MUSCL scheme with the Van-Albada TVD limiter, together with a reference curve obtained using 10,000 cells and the first-order HLLC scheme, are compared in Fig. 1 at $t = 1$ ms with $CFL = 0.8$. A significant improvement is clearly visible using either one of the 5th-order schemes compared to MUSCL, but the TENO scheme yields the most accurate result. Hereafter, the effect of user-defined threshold parameter C_T is studied for $C_T = 10^{-2}, 10^{-4}$ and 10^{-7}, and compared with the reference curve and the solution obtained by WENO-Z, corresponds to conceding the strict demand of ENO-like stencil selection. Increasing C_T corresponds to enhancing the ENO property and robustness of the scheme, however, it results in decreasing spatial accuracy. In the limit of $C_T \to 0$, the TENO scheme becomes a modified version of WENO-Z. Fig. 2 displays this comparison for both the pressure and gas void fraction, near the left rarefaction wave and the domain center, respectively. The TENO solution with $C_T < 10^{-3}$ is superior in comparison to the WENO-Z solution for the current benchmark case. Furthermore, the TENO scheme appears very suitable for capturing cavitation onset without introducing artificial oscillations.

4.3. Shock tube problem

The third one-dimensional benchmark case considered here is a 1m long shock-tube filled with high pressure liquid water on the left side, and air at atmospheric pressure on the right side. A

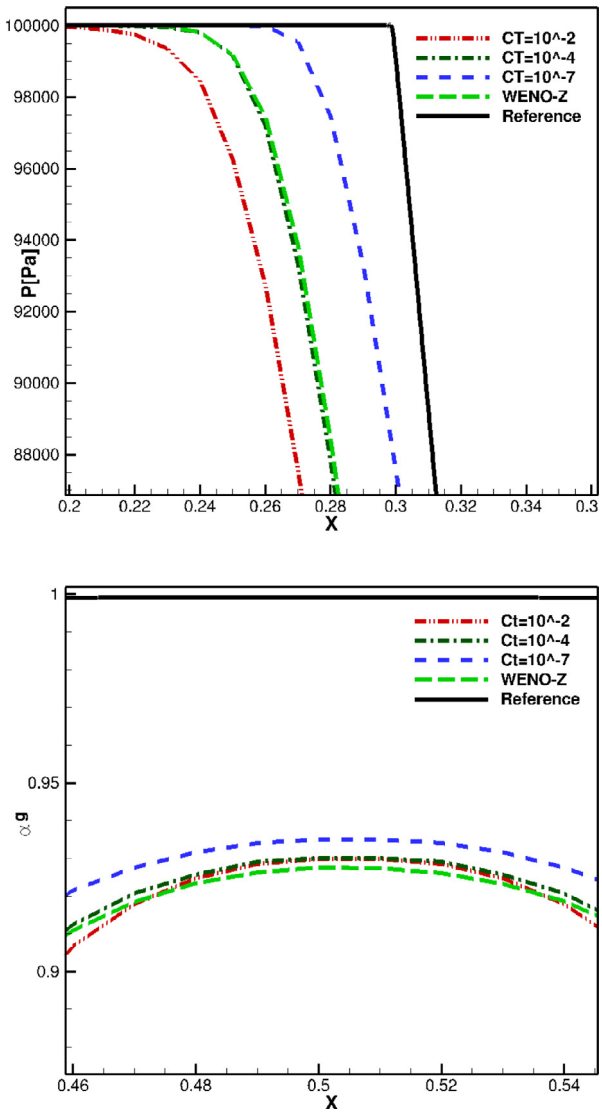

Fig. 2. Effect of TENO threshold parameter C_T and comparison with WENO-Z solution for pressure and void fraction obtained at $t = 1$ ms.

diaphragm is initially located at $x = 0.7$m, and the EOS parameters for each fluid are $\gamma_g = 1.4, P_{\infty,g} = 0$ for air and $\gamma_l = 4.4, P_{\infty,l} = 6 \cdot 10^8$ Pa for liquid. The initial conditions are given as follows:

$$(P, \alpha_g, \rho_g, \rho_l, u_g, u_l)_L = (10^9, \epsilon, 50, 1000, 0, 0)$$

$$(P, \alpha_g, \rho_g, \rho_l, u_g, u_l)_R = \left(10^5, 1-\epsilon, 50, 1000, 0, 0\right)$$

A comparison between the 5th-order TENO scheme with $C_T = 10^{-4}$, the 5th-order WENO-JS, the 3rd order MUSCL and the exact solution is presented in Fig. 3, where the computational domain is discretized using 100 cells with $CFL = 0.25$ and the solution is obtained at $t = 229$ μs. Note that both the pressure and void fraction gradients are relatively large for this case, resulting in the source term $P\frac{\partial \alpha_g}{\alpha_g}$ introducing numerical stiffness in contrast with other cases studied herein. For practical consideration of numerical implementation, a small void fraction of $\epsilon = 10^{-6}$ must be assigned. Negligible differences are observed between the WENO-JS and TENO results for this case, although substantial improvement is achieved when using a high-order scheme, as compared with the results obtained with the six equation model by Yeom and Chang [46] and Paillere et al. [33] using the HLLC and AUSM+ approximate Riemann solver, respectively, and the seven-equation model by Saurel and Abgrall [37] and Saurel and Lemetayer [38].

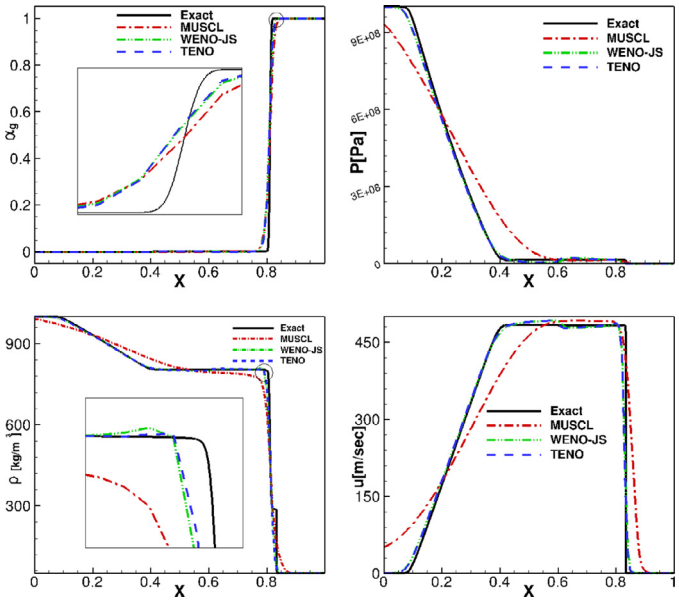

Fig. 3. Comparison between TENO, WENO-JS, MUSCL and the exact solution for a one-dimensional shock-tube problem using 100 cells, $CFL = 0.25, t = 229\ \mu s$, displaying gas void fraction, pressure, mixture density and velocity.

In the vicinity of the right travelling shock wave near $x = 0.8$, a small artificial oscillation can be discerned in the mixture density value with the WENO-JS scheme, nevertheless, this difference from the exact solution is local and relatively small compared with the MUSCL scheme results. This oscillation is prevented when employing the TENO scheme, as shown in Fig. 3. It is also noted that the bump seen in the velocity and pressure solutions at $x = 0.6$ vanishes as the spatial resolution increases. Many researchers prefer to present their predictions for this benchmark case using 1000 cells or choosing the pressure ratio to be 10^3, which does not adequately demonstrate the strength of their scheme.

In the region of the left travelling rarefaction wave, both high-order schemes, namely WENO-JS and TENO, produce excellent agreement with the exact solution. Regarding all other physical quantities, a slight improvement is observed utilizing TENO as compared with WENO-JS.

For strong pressure ratio problems, such as the shock tube problem with pressure ratio of 10^4, it appears the TENO scheme is able to produce highly accurate results in comparison with all the other schemes presented here.

4.4. Multiphase interface test

In this first two-dimensional test case, the capabilities of the implemented TENO scheme to retain high-order spatial accuracy without introducing spurious oscillations are tested by simulating the advecting two phase interface test case. We follow the initial condition of Shyue [39], where a circular cylindrical interface with radius $r_0 = 0.16m$ and velocity $(u, v) = (1, 1)$ are specified. The initial physical parameters of each fluid are:

$$(\rho, \gamma, P_\infty) = \begin{cases} 1, 1.4, 0 & r \le r_0 \\ 0.125, 4, 1 & r > r_0 \end{cases} \tag{43}$$

with an initial pressure distribution of unity over the entire square computational domain with edge size $1m$. A uniform grid of 100×100 cells is used with a $CFL = 0.6$.

Gas void fraction contours plots are presented in Fig. 4 from 5th-order WENO-JS, 5th order TENO with $C_T = 10^{-4}$, 3rd-order MUSCL-TVD scheme, and the exact solution denoted by the dashed circle, all presented at $t = 0.36$ s. Low-order spatial reconstruction schemes, such as MUSCL, typically result in a relatively large

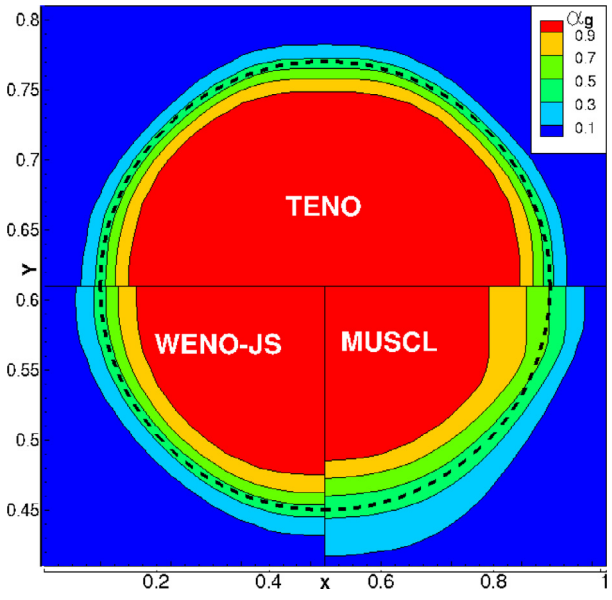

Fig. 4. A composite figure comparing gas void fraction contour plots captured at $t = 0.36$ s, between 5th-order TENO with $C_T = 10^{-4}$ (upper half), 5th-order WENO-JS (lower left quarter) and 3rd-order MUSCL (lower right quarter). Exact solution is indicated by dashed line.

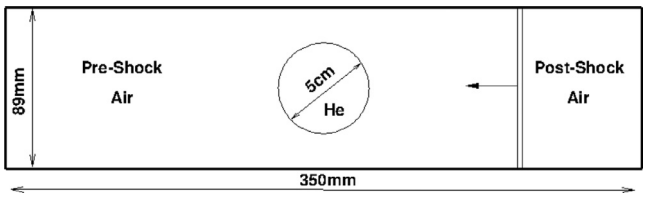

Fig. 5. Setup of the He/air shock-bubble interaction.

smearing bandwidth. It is observed that both 5th-order schemes can successfully capture the interface zone without introducing artificial instabilities, but with the TENO reconstruction a sharper interface zone is achieved as compared to WENO-JS.

4.5. Air/He shock-bubble interaction

In this section, a Helium bubble with density lighter than the air surrounding it and a planar shock wave moving towards the bubble interact as depicted in Fig. 5. Haas and Sturtevant [18] performed experiments for this Helium bubble-air shock interaction case and many researchers have used this case to numerically validate their own solvers including Quirk and Karni [36] using an interface-capturing method, Coralic and Colonius [10] using a multicomponent version of the reduced five-equation model and a 5th-order WENO-JS scheme, the five-equation multiphase model as implemented by Ansari and Daramizadeh [3] and seven-equation adaptation implemented on a GPU by Liang et al. [27].

The computational domain is 350 mm long and 89 mm wide with a Helium bubble of 5 cm diameter initially located in the middle and the shock velocity is $M = 1.22$. The initial conditions are:

$$(P, \rho, u, v, \gamma, P_\infty) = \begin{cases} 1.5698\ 10^5\ \text{Pa}, 1.92691\ \frac{\text{kg}}{\text{m}^3}, -113.5\ \frac{\text{m}}{\text{sec}}, \\ \quad 0\ \frac{m}{sec}, 1.4, 0\ Pa & \text{Post-shock}, \\ 10^5\ \text{Pa}, 1.4\ \frac{\text{kg}}{\text{m}^3}, 0\ \frac{\text{m}}{\text{sec}}, 0\ \frac{\text{m}}{\text{sec}}, 1.4, 0\ \text{Pa} & \text{Pre-shock}, \\ 10^5\ \text{Pa}, 0.25463\ \frac{\text{kg}}{\text{m}^3}, 0\ \frac{\text{m}}{\text{sec}}, 0\ \frac{\text{m}}{\text{sec}}, \\ \quad 1.648, 0\ Pa & \text{Helium bubble} \end{cases} \tag{44}$$

Transmissive boundary conditions are used for both left and right boundaries and reflective conditions are used for both top and

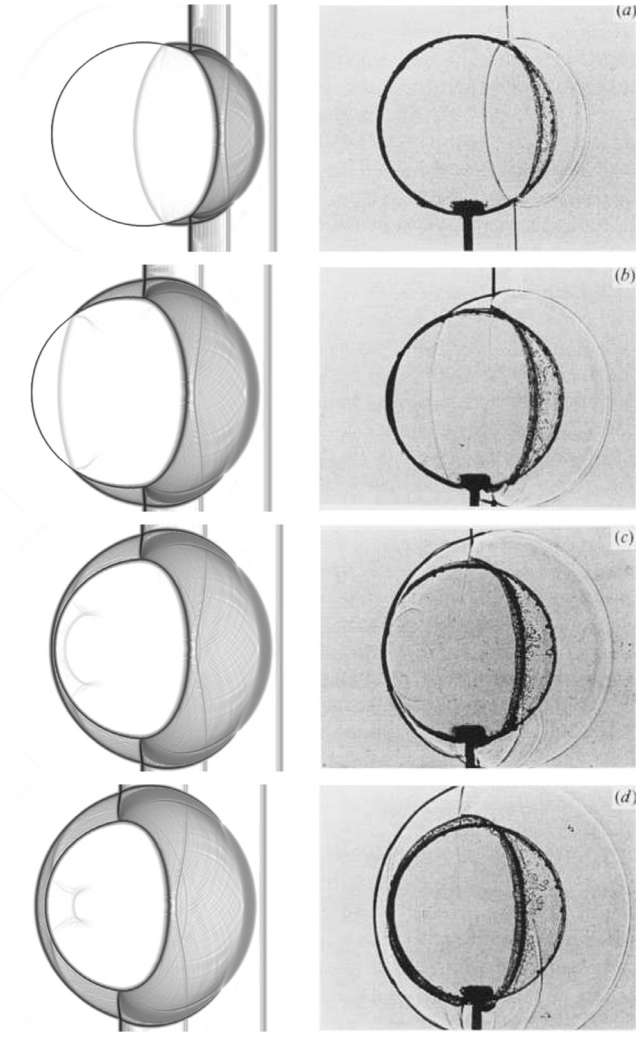

Fig. 6. Comparison between Schlieren plots from experiments conducted by Haas and Sturtevant [18] (right) and numerical results in the Helium-air shock bubble interaction case. (a) $t = 32$ μs. (b) $t = 52$ μs. (c) $t = 62$ μs. (d) $t = 72$ μs. Reproduced with permission from Cambridge University Press.

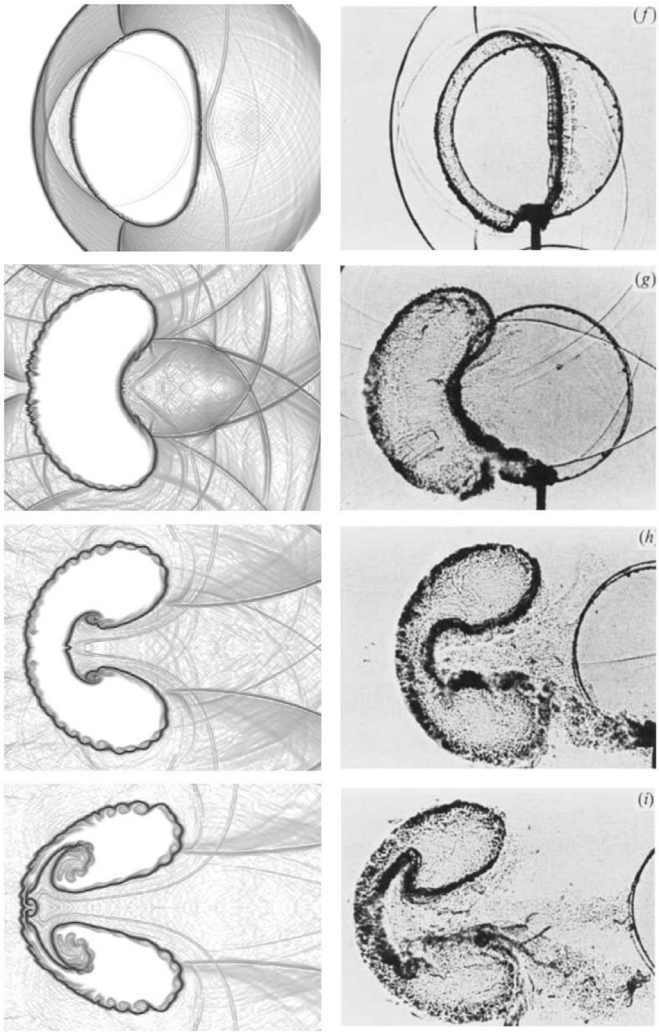

Fig. 7. Comparison between Schlieren plots from experiments conducted by Haas and Sturtevant [18] (right) and numerical results in the Helium-air shock bubble interaction case. (f) $t = 102$ μs. (g) $t = 245$ μs. (h) $t = 427$ μs. (i) $t = 674$ μs. Reproduced with permission from Cambridge University Press.

bottom boundaries to mimic solid walls as in the experiments [18]. The domain is discretized using a uniform grid of 2000×500 cells resulting in a spatial resolution of $\Delta x = 175$ μm and $\Delta y = 178$ μm with $CFL = 0.4$.

To accentuate fine flow details, we present density gradient magnitude plots, also known as numerical Schlieren-type images, calculated by $log(|\nabla \rho_m| + 1)$. Figs. 6 and 7 depict a qualitative comparison of these Schlieren-type images with the experimental results of [18] with our 5th-order TENO scheme with $C_T = 10^{-4}$, captured at approximately the same time.

Since the sound speed in the helium bubble is higher than the air surrounding it, the transmitted shock inside the bubble travels faster than the incident shock, as seen by two vertical lines outside the bubble in Fig. 6(a), simultaneously with the emergence of expansion fan. The intricate interaction of the incident, transmitted, and reflected shocks with the accompanied expansion fan is clearly seen in Fig. 6(c). Moreover, the Kelvin–Helmholtz instability, responsible for air-jet evolution along the interface, is well captured in Fig. 7(g) and (h). The scheme manages to capture small scale vortices along the He-air interface in contrast with results obtained with low order schemes having similar spatial resolution.

Several wave velocities have also been calculated from the simulation results including the incident, refracted, upstream interface, downstream interface, and jet velocities to more quantitatively assess our scheme. We follow the notation of Haas and Sturtevant [18] regarding the names of the various waves and find all calculated velocities are within the 10% error bar of the experiment, as displayed in Table 2.

Table 2
Comparison between several velocities obtained using 5th-order TENO scheme and experimental measurements conducted by Haas and Sturtevant [18].

Velocity	TENO (m/s)	Experiment [18] (m/s)
Incident	400	410 ± 41
Refracted	863	900 ± 90
Upstream interface	167	170 ± 17
Downstream interface	137	145 ± 15
Jet	222	230 ± 23

4.6. Water/Air shock bubble interaction

In this section, a shock-bubble interaction problem featuring a water-air multiphase fluid with a large density ratio is studied. This case has been investigated by Chang and Liou [8] using AUSM+up Riemann solver and the six-equation two-fluid formulation, and

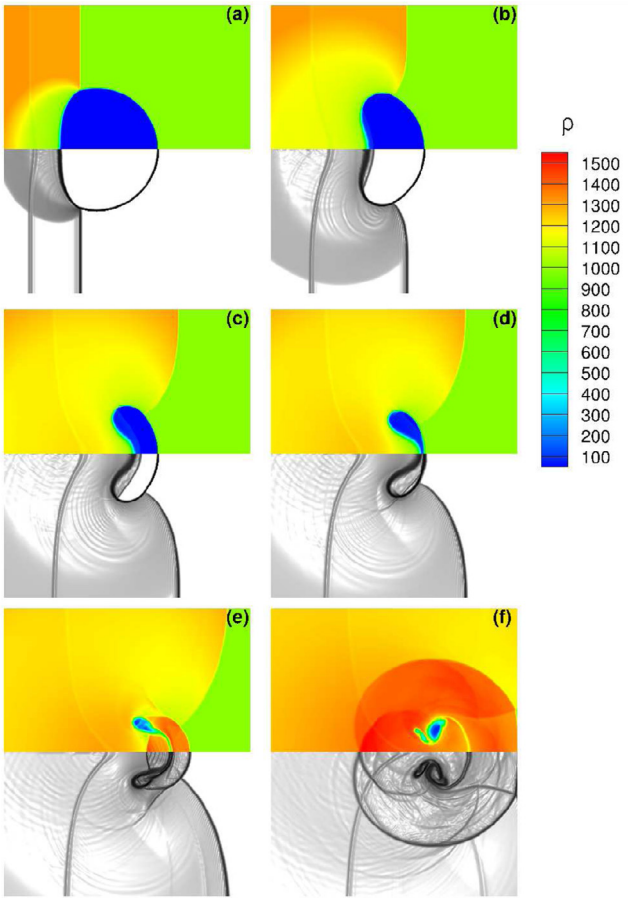

Fig. 8. Density (top) and numerical Schlieren images (bottom) of water-air shock bubble interaction at (a) $t = 1.2$ μs, (b) $t = 2.3$ μs, (c) $t = 3.0$ μs, (d) $t = 3.4$ μs, (e) $t = 3.9$ μs, (f) $t = 5.0$ μs.

in what follows it was solved with a modified pressure-velocity based diffusion term by Niu [31]. Utilizing a hyperbolic tangent function coupled with the governing equations may enhance spatial resolution as demonstrated by Nonomura et al. [32]. Ansari and Daramizadeh [3] also simulated this case using the reduced five-equation multiphase model. All the above mentioned papers= employed a low-order spatial reconstruction.

Here, we consider an air bubble immersed in water where the shock wave travels towards the bubble. The domain dimensions are $L_x = L_y = 0.024$m and a uniform grid of 800 × 800 computational cells are employed, results in spatial resolution of 30 μm. The initial radius of the air bubble is 3 mm and is located in the middle of the domain. The initial conditions are given by:

$$(P, \rho, u, v, \gamma, P_\infty) = \begin{cases} 1.6\ 10^9\ \text{Pa}, 1323.65\ \frac{\text{kg}}{\text{m}^3}, 661.81\ \frac{\text{m}}{\text{sec}}, \\ \quad 0\ \frac{m}{sec}, 4.4, 6\ 10^8\ \text{Pa} & \text{Post-shock}, \\ 10^5\ \text{Pa}\ , 1000\ \frac{\text{kg}}{\text{m}^3}, 0\ \frac{\text{m}}{\text{sec}}, 0\ \frac{\text{m}}{\text{sec}}, 4.4, 6\ 10^8\ \text{Pa} & \text{Pre-shock}, \\ 10^5\ \text{Pa}, 1.0\ \frac{\text{kg}}{\text{m}^3}, 0\ \frac{\text{m}}{\text{sec}}, 0\ \frac{\text{m}}{\text{sec}}, 1.4, 0\ \text{Pa} & \text{Air bubble} \end{cases} \tag{45}$$

In Fig. 8 the time evolution of both density (top) and contours of numerical Schlieren (bottom) are presented. As the shock wave hits the air bubble, the evolution of a strong reflected radial rarefaction wave is clearly visible in Fig. 8(a) and (b). Over time, the rarefaction waves contribute to the evolution of a high-speed centerline water-jet, with typical axial velocity of 2450 ms. This water-jet is responsible for deforming the air bubble into a crescent-type shape, and eventually separating it into two disconnected gas bubbles, as depicted in Fig. 8(c) and (d). Hereafter, a collision between still water and the water-jet results in the emergence of a shock wave, radially expanding as seen in Fig. 8(e) and (f).

4.7. Underwater explosion near water-air surface

Based on numerous underwater explosion experiments, Kedrinskii [25] concluded the shock wave front pressure is generally dependent on the reduced distance parameter, $r^0 = \frac{r_{fr}}{\sqrt{Q}}$, where r_{fr} is the cylindrical wave front radius and Q is the released energy per unit length. Following the above finding, we consider a $2D$ underwater explosion of 10 mg Silver Azide (AgN_3) having an initial energy of 25.5 J/m, modeled as a high pressure liquid sphere core with radius of 1 cm, and experimental Schlieren-type images were produced by Kleine et al. [26]. The domain dimensions are 0.35 m × 0.35 m, with the water-air interface located in the middle and the explosive core is located 5cm below the interface. A non-uniform mesh consisting of 500 × 500 cells with $CFL = 0.6$ is used.

Recently, the above problem was simulated by Petrov and Schmidt [35] using an Eulerian–Lagrangian approach having a carrier and dispersed phase and by Daramizadeh and Ansari [12] using the reduced five-equation model of Allaire et al. [2]. Both of these studies were carried out employing low-order spatial discretization.

Fig. 9 depicts a qualitative comparison between Schlieren-type plots from experiments conducted by Kleine et al. [26] and from our numerical simulations using the 5th-order TENO scheme, presented at 14,28 and 42 μs, from top to bottom, respectively. At early times, a radial shock wave expands towards the water-air interface, as presented in Fig. 9(a). Due to the large acoustic impedance ratio across the interface, a strong reflective shock wave travels back towards the bubble expansion zone, whereas a minor wave is transmitted to the ambient air, as shown in Fig. 9(b). Hereafter, a cavitation region has emerged below the water-air interface where finer details representing the intricate dynamics are clearly observable. It is noteworthy that the high velocity reflected wave is responsible for cavitation emergence below the surface, where high kinetic energy results in low pressure, as demonstrated by the corresponding stiffened-gas equation of state. Velocity magnitude contours plots are presented in the left column of Fig. 9, where high velocity magnitude corresponds to cavitation emergence.

4.8. Cylindrical underwater explosion near a rigid surface

In the second underwater explosion case, the interaction between a shock wave emanating from an expanding gas bubble and a rigid surface covering the upper boundary is considered. Xie et al. [44] employed a one-fluid model with a modified ghost-fluid method to take into consideration elastic boundaries and to study the effect of various initial depths of explosive gas bubbles and the compressibility of the upper wall. Recently, Ma et al. [29] studied this problem, using the reduced multiphase five-equation model and incorporated with a MUSCL scheme. In our study, the domain is discretized using 360 × 270 uniform computational cells and $CFL = 0.6$. Following [44], the initial explosive gas bubble radius is $1m$ and its core located 3m below the water-air surface:

$$(P, \rho, u, v, \gamma, P_\infty) = \begin{cases} 8.29 \cdot 10^8\ \text{Pa}, 1270\ \text{Kg/m}^3, 0\ \text{m/sec}, \\ \quad 0\ \text{m/sec}, 2.0, 0 & \text{Explosive gas}, \\ 10^5\ \text{Pa}, 1\ \text{Kg/m}^3, 0\ \text{m/sec}, 0\ \text{m/sec}, 2.0, 0 & \text{Air}, \\ 10^5\ \text{Pa}, 1000\ \text{Kg/m}^3, 0\ \text{m/sec}, 0\ \text{m/sec}, 7.5, \\ \quad 3 \cdot 10^8\ Pa & \text{Water} \end{cases} \tag{46}$$

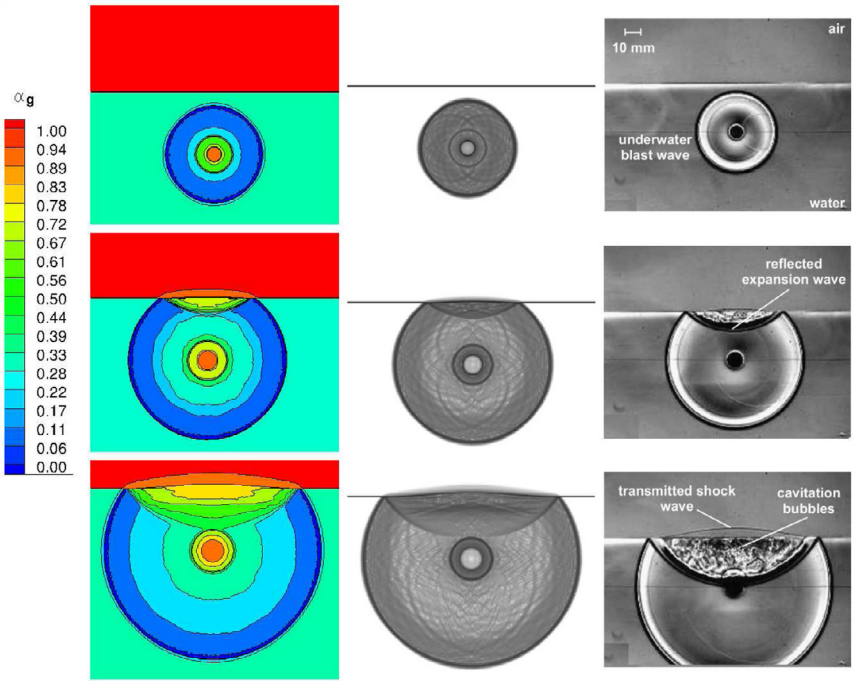

Fig. 9. Comparison between density-based Schlieren-type images experimentally obtained by Kleine et al. [26] (right column) and 5th-order TENO scheme numerical results (middle column) at 14, 28 and 42 μs for the AgN_3 underwater explosion case. Velocity magnitude plots are shown in the left column. Reproduced with permission from Springer.

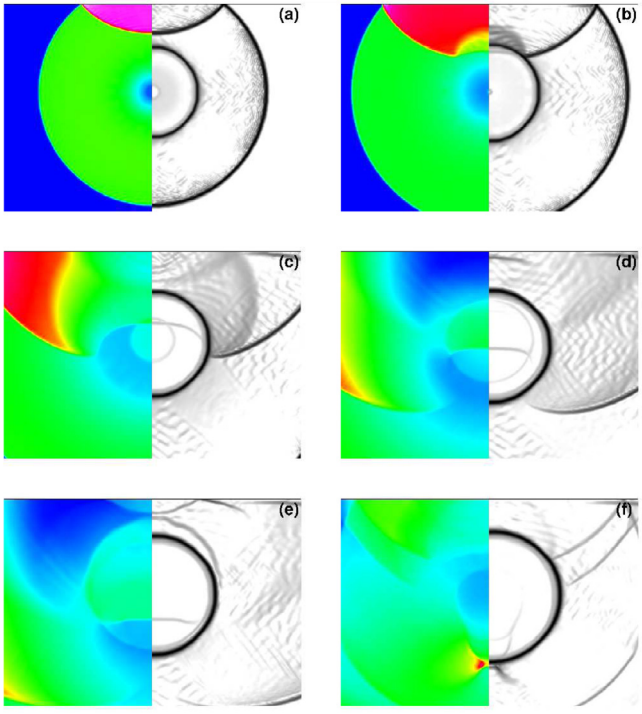

Fig. 10. Numerical Schlieren-type plots (right) and pressure contours (left) in the underwater explosion case under a rigid surface obtained at (a) $t = 1.5$ ms, (b) $t = 2.0$ ms, (c) $t = 3.0$ ms, (d) $t = 4.0$ ms, (e) $t = 5.0$ ms and (r) $t = 7.0$ ms.

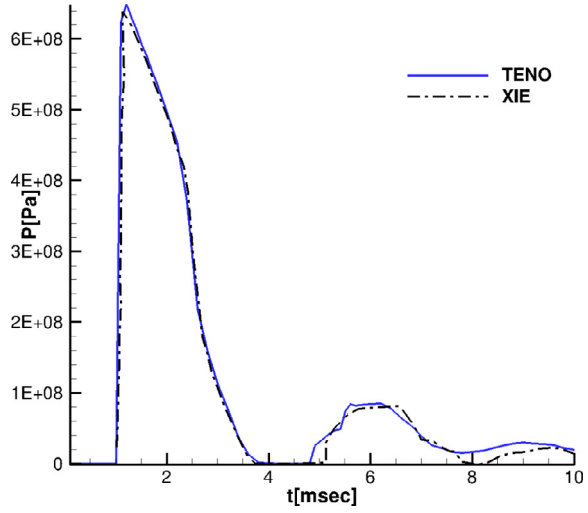

Fig. 11. Pressure time history comparison at the middle point of the upper rigid wall between TENO scheme predictions and the one-fluid model of Xie et al. [44].

Each time frame in Fig. 10 presents both pressure contours (left half) and Schlieren-type images (right half). Initially, high-pressure waves expand radially from the gas core and the reflected shock wave from the upper rigid surface is clearly visible in Fig. 10(a). Subsequently, the reflected shock collides with the expanding gas core and an expansion fan wave is created and evolves, as shown in Fig. 10(b). In Fig. 10(c) and (d), the development of a low-pressure cavitation zone under the rigid surface, formed due to the reflection of the rarefaction wave, can be seen. Thereafter, as shown in Fig. 10(e), after approximately 4.9 ms, the cavitation zone collapses and a secondary shock wave evolves and travels towards the gas bubble. Ultimately, the repetitive progression of cavitation zone inception and its collapse weakens with time, see Fig. 10(f).

The time-history of the pressure at the middle point of the upper rigid surface is presented in Fig. 11 and compared with [44]. The first pressure peak resulting from the initial expanding shock wave is 645 MPa according to our simulation, in comparison with 628 MPa from Xie et al. [44] and 700 MPa from Ma et al. [29]. In our simulations, the cavitation collapse time starts 0.2 ms before

the prediction of Xie et al. [44] at 5.1 ms, and a similar preceding time interval was reported by Ma et al. [29]. The pressure peak of the secondary shock wave following the cavitation zone collapse is 82 MPa, which is 6% higher than the calculated pressure peak by Xie et al. [44].

5. Conclusions

A robust high-order finite-volume numerical scheme for simulating multicomponent and multiphase flows has been implemented and tested. It is based on a novel targeted-ENO (TENO) reconstruction scheme, which enhances the ENO property and improves convergence properties near extrema points resulting in well-resolved simulations of complex flow features without spurious oscillations. The scheme is successfully demonstrated on a range of challenging 1*D* and 2*D* problems. Our findings indicate that the TENO-based scheme is less dissipative than both the WENO-Z and WENO-JS versions. Implementation of a high-order positivity-preserving limited is the underway and will be the subject of future studies.

Acknowledgment

The authors would like to acknowledge financial support for this research from the Technion.

Appendix A. Derivation of WENO scheme weights

A mathematical derivation of the polynomials and ideal weights associated with a 5th-order WENO scheme together with modifications for the WENO-Z and TENO schemes is described in this appendix.

$$V^{L}_{i+1/2} = \sum_{r=0}^{k-1} \omega^{L,(r)}_{i+1/2} V^{L,(r)}_{i+1/2} = V(x_{i+1/2}) + O(\Delta x)^5 \tag{A.1}$$

$V^{(r)}(x)$ where the Lagrange form in each stencil is:

$$V^{(r)}(x) = \sum_{m=0}^{k} \sum_{j=0}^{m-1} V_{i-r+j} \Delta x_{i-r+j} \frac{\sum_{l=0}^{k} \prod_{q=0}^{k} (x - x_{i-r+q-1/2})}{\prod_{l=0}^{k} (x_{i-r+m-1/2} - x_{i-r+l-1/2})} \tag{A.2}$$

where V_i is the primitive cell average values to reconstruct and r indicates the left shift and varies in the range of $r = 0, 1, 2$, for a 5th-order reconstruction at the cell face $i + 1/2$ the result is:

$$V^{L,(0)}_{i+1/2} = \frac{2V_i + 5V_{i+1} - V_{i+2}}{6} \tag{A.3a}$$

$$V^{L,(1)}_{i+1/2} = \frac{-V_{i-1} + 5V_i + 2V_{i+1}}{6} \tag{A.3b}$$

$$V^{L,(2)}_{i+1/2} = \frac{2V_{i-2} - 7V_{i-1} + 11V_i}{6} \tag{A.3c}$$

the 5th-order central scheme is obtained by substituting $k = 5$ and $r = 0$ in Eq. (A.2), evaluated at $x + 1/2$

$$\frac{2V_{i-2} - 13V_{i-1} + 47V_i + 27V_{i+1} - 3V_{i+2}}{60} \tag{A.4}$$

and the ideal weights are calculated by matching:

$$d^{L,(0)}_{i+1/2} = 3/10 \tag{A.5a}$$

$$d^{L,(1)}_{i+1/2} = 6/10 \tag{A.5b}$$

$$d^{L,(2)}_{i+1/2} = 1/10 \tag{A.5c}$$

Symmetrically, for $x_{i-1/2}$

$$V^{R,(0)}_{i-1/2} = \frac{11V_i - 7V_{i+1} + 2V_{i+2}}{6} \tag{A.6a}$$

$$V^{R,(1)}_{i-1/2} = \frac{2V_{i-1} + 5V_i - V_{i+1}}{6} \tag{A.6b}$$

$$V^{R,(2)}_{i-1/2} = \frac{-V_{i-2} + 5V_{i-1} + 2V_i}{6} \tag{A.6c}$$

and for the 5th-order central scheme:

$$\frac{-3V_{i-2} + 27V_{i-1} + 47V_i - 13V_{i+1} + 2V_{i+2}}{60} \tag{A.7}$$

and the ideal weights are calculated by matching:

$$d^{R,(0)}_{i-1/2} = 1/10 \tag{A.8a}$$

$$d^{R,(1)}_{i-1/2} = 6/10 \tag{A.8b}$$

$$d^{R,(2)}_{i-1/2} = 3/10 \tag{A.8c}$$

For a 5th-order accurate we utilize two Gauss–Legendre quadrature points:

$$l_{1,2} = x_i \pm \frac{\Delta x}{2\sqrt{3}} \tag{A.9}$$

$$V^{(0)}_{l_1} = \frac{-3\left(-4 + \sqrt{3}\right)V_i + 4\sqrt{3}V_{i+1} - \sqrt{3}V_{i+2}}{12} \tag{A.10a}$$

$$V^{(1)}_{l_1} = \frac{-\sqrt{3}V_{i-1} + 12V_i + \sqrt{3}V_{i+1}}{12} \tag{A.10b}$$

$$V^{(2)}_{l_1} = \frac{\sqrt{3}V_{i-2} - 4\sqrt{3}V_{i-1} + 3\left(4 + \sqrt{3}\right)V_i}{12} \tag{A.10c}$$

central polynomial evaluated at l_1

$$\frac{(-1+70\sqrt{3})V_i - 2 + (4 - 500\sqrt{3})V_{i-1} + 4314V_i + (4 + 500\sqrt{3})V_{i+1} - (1 + 70\sqrt{3})V_{i+2}}{4320} \tag{A.11}$$

corresponding ideal weights:

$$d^{(0)}_{l_1} = \frac{\sqrt{3} + 210}{1080} \tag{A.12a}$$

$$d^{(1)}_{l_1} = 11/18 \tag{A.12b}$$

$$d^{(2)}_{l_1} = \frac{-\sqrt{3} + 210}{1080} \tag{A.12c}$$

$$V^{(0)}_{l_2} = \frac{3\left(4 + \sqrt{3}\right)V_i - 4\sqrt{3}V_{i+1} + \sqrt{3}V_{i+2}}{12} \tag{A.13a}$$

$$V^{(1)}_{l_2} = \frac{\sqrt{3}V_{i-1} + 12V_i - \sqrt{3}V_{i+1}}{12} \tag{A.13b}$$

$$V^{(2)}_{l_2} = \frac{-\sqrt{3}V_{i-2} + 4\sqrt{3}V_{i-1} - 3\left(-4 + \sqrt{3}\right)V_i}{12} \tag{A.13c}$$

central polynomial evaluated at l_2

$$\frac{-(1+70\sqrt{3})V_i - 2 + (4+500\sqrt{3})V_{i-1} + 4314V_i + (4-500\sqrt{3})V_{i+1} - (-1+70\sqrt{3})V_{i+2}}{4320} \tag{A.14}$$

corresponding ideal weights:

$$d_{l_2}^{(0)} = \frac{-\sqrt{3}+210}{1080} \tag{A.15a}$$

$$d_{l_2}^{(1)} = 11/18 \tag{A.15b}$$

$$d_{l_2}^{(2)} = \frac{\sqrt{3}+210}{1080} \tag{A.15c}$$

References

[1] Abgrall R. How to prevent pressure oscillations in multicomponent flow calculations: a quasi conservative approach. J Comput Phys 1996;125:150–60.
[2] Allaire G, Clerc S, Kokh S. A five-equation model for the simulation of interfaces between compressible fluids. J Comput Phys 2002;181:577–616.
[3] Ansari MR, Daramizadeh A. Numerical simulation of compressible two-phase flow using a diffuse interface method. Int J Heat Fluid Flow 2013;42:209–23.
[4] Balsara DS, Shu CW. Monotonicity preserving weighted essentially non-oscillatory schemes with increasingly high order of accuracy. J Comput Phys 2000;160:405–52.
[5] Benson DJ. Computational methods in lagrangian and eulerian hydrocodes. Comput Methods Appl Mech Eng 1992;99:235–394.
[6] Bestion D. The physical closure laws in the CATHARE code. Nucl Eng Des 1990;124:229–45.
[7] Borges R, Carmona M, Costa B, Don WS. An improved weighted essentially non-oscillatory scheme for hyperbolic conservation law. J Comput Phys 2008;227:3191–211.
[8] Chang CH, Liou MS. A robust and accurate approach to computing compressible multiphase flow: stratified flow model and AUSM + -up scheme. J Comput Phys 2007;25:840–73.
[9] Cocchi JP, Saurel R. A riemann problem based method for the resolution of compressible multimaterial flows. J Comput Phys 1997;137:265–98.
[10] Coralic V, Colonius T. Finite-volume WENO scheme for viscous compressible multicomponent flows. J Comput Phys 2014;274:95–121.
[11] Davis SF. Simplified second order godunov type methods. SIAM J Sci Stat Comput 1988;9(3):445–73.
[12] Daramizadeh A, Ansari MR. Numerical simulation of underwater explosion near airwater free surface using a five-equation reduced model. Ocean Eng 2015;110:25–35.
[13] Drew DA. Mathematical modeling of two-phase flow. Ann Rev Fluid Mech 1983;291:15–261.
[14] Feng H, Hu FX, Wang R. A new mapped weighted essentially non-oscillatory scheme. J Sci Comput 2012;51:449–73.
[15] Fu L, Hu XY, Adams NA. A family of high-order targeted ENO schemes for compressible-fluid simulations. J Comput Phys 2016;305:333–59.
[16] Gottlieb S, Shu CW. Total variation diminishing rungekutta schemes. Math Comput 1998;67:73–85.
[17] Greenough JA, Rider WJ. A quantitative comparison of numerical methods for the compressible euler equations: fifth-order WENO and piecewise-linear godunov. J Comput Phys 2004;196:259–81.
[18] Haas JF, Sturtevant B. Interaction of weak shock waves with cylindrical and spherical gas inhomogeneities. J Fluid Mech 1987;181:41–76.
[19] Harlow F, Amsden A. Fluid dynamics. Technical report LA-4700. LANL; 1971.
[20] Harten A, Engquist B, Osher S, Chakravarthy S. Uniformly high order essentially non-oscillatory schemes III. J Comput Phys 1987;71:231–303.
[21] Henrick AK, Aslam TD, Powers JM. Mapped weighted essentially non-oscillatory schemes: achieving optimal order near critical points. J Comput Phys 2005;207:542–67.
[22] Jiang GS, Shu CW. Efficient implementation of weighted ENO schemes. J Comp Phys 1996;126:202–28.
[23] Johnsen E, Colonius T. Implementation of WENO schemes in compressible multicomponent flow problems. J Comput Phys 2006;219:715–32.
[24] Kapila AK, Menikoff R, Bdzil JB, Son SF, Stewart DS. Two-phase modeling of deflagration-to-detonation transition in granular materials: reduced equations. Phys Fluids 2001;13:3002–24.
[25] Kedrinskii VK. Hydrodynamics of explosion:experiments and models. Berlin: Springer; 2004.
[26] Kleine H, Tepper S, Takehara K, Etoh TG, Hiraki H. Cavitation induced by low-speed underwater impact. Int J Shock Waves 2009;19:895–900.
[27] Liang S, Liu W, Yuan L. Solving seven-equation model for compressible two-phase flow using multiple GPUs. Comput Fluids 2014;99:156–71.
[28] Luo H, Baum JD, Lohner R. On the computation of multi-material flows using ALE formulation. J Comput Phys 2004;194:304–28.
[29] Ma ZH, Causon DM, Qian L, Gu HB, Mingham CG, Ferrer PM. A GPU based compressible multiphase hydrocode for modelling violent hydrodynamic impact problems. Comput Fluids 2015;120:1–23.
[30] Miller GH, Puckett EG. A high-order godunov method for multiple condensed phases. J Comput Phys 1996;128:134–64.
[31] Niu YY. Computations of two-fluid models based on a simple and robust hybrid primitive variable riemann solver with AUSMD. J Comput Phys 2016;308:389–410.
[32] Nonomura T, Kitamura K, Fujii K. A simple interface sharpening technique with a hyperbolic tangent function applied to compressible two-fluid modeling. J Comput Phys 2014;258:95–117.
[33] Paillere H, Corre C, Cascales JRG. On the extension of the AUSM+ scheme to compressible two-fluid models. Comput Fluids 2003;32:891–916.
[34] Perigaud G, Saurel R. A compressible flow model with capillary effects. J Comput Phys 2005;209:139–78.
[35] Petrov NV, Schmidt AA. Multiphase phenomena in underwater explosion. Exp Therm Fluid Sci 2015;60:367–73.
[36] Quirk JJ, Karni S. On the dynamics of a shock-bubble interaction. J Fluid Mech 1996;318:129–63.
[37] Saurel R, Abgrall R. A multiphase godunov method for compressible multifluid and multiphase flows. J Comput Phys 1999;150:425–67.
[38] Saurel R, Lemetayer O. A multiphase model for compressible flows with interfaces, shocks, detonation waves and cavitation. J Fluid Mech 2001;431:239–71.
[39] Shyue KM. An efficient shock-capturing algorithm for compressible multicomponent problems. J Comput Phys 1998;142:208–42.
[40] Stewart H, Wendroff B. Two phase flow: models and methods. J Comput Phys 1984;56:363–409.
[41] Stuhmiller J. The influence of interfacial pressure forces on the character of two-phase flow model equations. Int J Multiphase Flow 1977;3:551–60.
[42] Titarev VA, Toro EF. Finite-volume WENO schemes for three-dimensional conservation laws. J Comput Phys 2004;201:238–60.
[43] Toro EF. Riemann solvers and numerical methods for fluid dynamics. Berlin: Springer; 1999.
[44] Xie WF, Young YL, Liu TG, Khoo BC. Dynamic response of deformable structures subjected to shock load and cavitation reload. Comput Mech 2007;40:667–81.
[45] Yeom GS, Chang KS. Numerical simulation of two-fluid two-phase flows by HLL scheme using an approximate jacobian matrix. Numer Heat Transfer B-Fund 2006;49:155–77.
[46] Yeom GS, Chang KS. A modified HLLC-type riemann solver for the compressible six-equation two-fluid model. Comput Fluids 2013;76:86–104.
[47] Zein A, Hantke M, Warnecke G. Modeling phase transition for compressible two-phase flows applied to metastable liquids. J Comput Phys 2010;229:2964–98.